Optical properties of $Pb_{0.52}Zr_{0.48}TiO_3$ nanorod arrays: second harmonic generation and multiphoton carrier dynamics

Journal of Physics: Photonics

PAPER

Optical properties of $Pb_{0.52}Zr_{0.48}TiO_3$ nanorod arrays: second harmonic generation and multiphoton carrier dynamics

Rathsara R H H Mudiyanselage[1,5], John Burton[1], Brenden A Magill[1], Kiara McMillan[1], Gabriella Gagliano[1], Ada J Morral[1], Min Gyu Kang[2,3,5], Han Byul Kang[2,3], Shashank Priya[2,3], Christopher J Stanton[4] and Giti A Khodaparast[1,*]

[1] Department of Physics, Virginia Tech, Blacksburg, VA 24061, United States of America
[2] Center for Energy Harvesting Materials and Systems (CEHMS), Virginia Tech, Blacksburg, VA 24061, United States of America
[3] Department of Materials Science and Engineering, Pennsylvania State University, University Park, PA 16802, United States of America
[4] Department of Physics, University of Florida, Gainesville, FL 32611, United States of America
[5] Authors with equal contributions
[*] Author to whom any correspondence should be addressed.

E-mail: khoda@vt.edu

Keywords: quantum sensing, PZT, second harmonic generation, nanorods, time resolved spectroscopy, multiferroics

OPEN ACCESS

RECEIVED
21 October 2020

REVISED
27 March 2021

ACCEPTED FOR PUBLICATION
27 April 2021

PUBLISHED
10 June 2021

Abstract

Nonlinear optical properties of poled and unpoled, lead zirconate-titanate ($Pb_{0.52}Zr_{0.48}TiO_3$) nanorod arrays, grown on Pt-coated Si with ∼200 nm diameter and ∼600 nm height, were investigated. Clear signatures of second harmonic generations (SHG), from 490–525 nm (2.38–2.53 eV) at room temperature, were observed. Furthermore, time resolved differential reflectivity measurements were performed to study dynamical properties of photoexcited carriers in the range of 690–1000 nm where multiphoton processes were responsible for the photo-excitations. We compared this excitation scheme, which is sensitive mainly to the surface states, to when the photoexcited energy (∼3.1 eV) was close to the band gap of the nanorods. Our results offer promises for employing these nanostructures in nonlinear photonic applications.

1. Introduction

Optoelectronic technologies, based on the second harmonic generation (SHG) effects, have been making impacts in devices such as ultrafast pulse laser generation [1], optical switches [2], modulators [3], materials analysis, and sensors [4–7]. Toward these advancements, employing low dimensional materials systems have attracted many research activities, aiming for more tunability, miniaturization, and integration on chips.

Beyond commonly used materials such as $LiNbO_3$, KDP, KTP, and BBO [8], low dimensional materials are being explored as promising alternatives to existing nonlinear optical materials. With the advancement in material engineering and material fabrication techniques, several emerging 2D structures have been studied including graphene [9], graphdiyne [10], 2D metal–organic frameworks (MOFs) [11], antimonene [12], and 2D transition-metal carbides [13], and carbonitrides [14].

Furthermore, for broader photonics applications it is significantly important to discover and explore materials with new functionalities. Ferroelectric nanostructures have been widely studied due to their broad range of applications where their piezoelectric and pyroelectric properties can be used in sensors [15, 16], actuators [17–21], transducers [22, 23], infrared detectors [20], and energy harvesting [23–30]. Our $Pb_{0.52}Zr_{0.48}TiO_3$ (PZT) nanorod arrays in this study, exhibit excellent coupling between electro-mechanical parameters and display polarization switching behavior along the growth direction, making them ideal candidates for nonvolatile memories [31–33].

Because the optical properties of these single crystalline PZT nanorod arrays are less explored, we study SHG, in which, for practical applications these nanorods can be easily grown on commercial silicon wafers to be compatible with existing semiconductor devices. We also used transient time-resolved differential reflectivity (TRDR) measurements to characterize the nature of carrier relaxation dynamics in this nanostructure. Near infrared (NIR) optical pulses were used, to probe multiphoton absorption, in which the

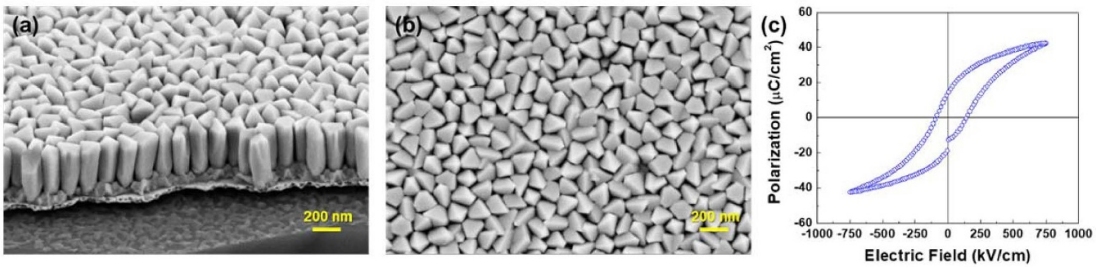

Figure 1. Cross-sectional FESEM image (a) and surface morphology (b) of PZT nanorod arrays. The array has a close-packed structure and is nearly homogeneous in diameter and height. (c) Polarization versus electric field (P-E) loop for the nanorod arrays displaying ferroelectric behavior.

relaxation dynamics are expected to be sensitive to the surface states. To directly probe the interband carrier dynamics, we employed near gap excitation at 400 nm. Probing these two schemes allowed us to probe several different relaxation mechanisms in these nanorod arrays.

2. Sample preparation and characterization

The PZT nanorod arrays were synthesized through the physical vapor growth method. The nanorods were grown on 20 nm diameter $La_{0.67}Sr_{0.33}MnO_3$ (LSMO) seeds, patterned on top of Pt coated Si(100) substrate through a polymer nano-template method, using RF sputtering at 400 °C. The microstructure of PZT nanorod arrays was observed using field-emission scanning electron microscopy (FESEM, LEO 1550). The PZT nanorod arrays were synthesized with ∼200 nm diameter and ∼600 nm height, as shown in figures 1(a) and (b). The PZT nanorods were found to have a close-packed structure and nearly homogeneous dimensions for diameter and height, grown on commercial grade 3 inch silicon wafers [31]. While each nanorod is a single crystal, the ensemble is composed of nanorods with random orientations. From x-ray diffraction (XRD) patterns, the nanorod arrays were found to exhibit perovskite phase without any secondary phases. The nanorod arrays exhibited randomly oriented diffraction peaks without preferred crystal orientation, which is often observed in the polycrystalline thin films due to the difference in the coefficient of thermal expansion between the substrate and thin film. The nano-structuring in PZT can overcome the influence of the substrate clamping effects [31].

The polarization-electric field (P-E) loop for the PZT nanorods was measured using a ferroelectric tester (Premier II, Radiant), and it was found that the nanorods exhibit typical ferroelectric behavior with remnant polarization of ∼16 $\mu C\,cm^{-2}$ (figure 1(c)). In order to induce the switching of the polarization direction of the nanorod arrays, the corona poling method was used [34]. A DC bias of 23 kV was applied between the Pt bottom electrode and a sharp tungsten tip placed 5 cm above the sample surface to generate a corona discharge through the partial breakdown of air. This method forms electrical charges on the sample surface and enables non-contact ferroelectric polarization switching over a large area.

3. SHG in PZT nanorods

Pulsed femtosecond lasers are suitable sources to observe nonlinear optical phenomena. The field generated by the incident light in a nonlinear medium gives rise to nonlinear effects like SHG where the electric field of the incident light results in an atomic dipole moment in the material. These nonlinear optical processes can be described macroscopically [35], by the induced polarization as following:

$$P(t) = P_0 + \varepsilon_0 \chi^{(1)} E(t) + \chi^{(2)} E^2(t) + \chi^{(3)} E^3(t) + \cdots \quad (1)$$

where P_0 is a constant polarization, the second term describes the linear response, and the higher order electric field terms describe the nonlinear optical response. The third term in equation (1) gives rise to second-order nonlinear optical phenomena, such as SHG, where $\chi^{(2)}$ is the second-order nonlinear electric susceptibility. The polarization is an odd function of electric field in a nonlinear material system with inversion symmetry (i.e. a centrosymmetric medium). Therefore, second-order nonlinear phenomena can only be observed in a medium where inversion symmetry is broken. In nanostructures, SHG can occur at grain boundaries, interfaces, and defects. Compared to thin films, in nanorods, the surface to volume ratio is higher, resulting in a higher surface SHG contribution, as the effective surface dipole moment is also higher [8, 36, 37].

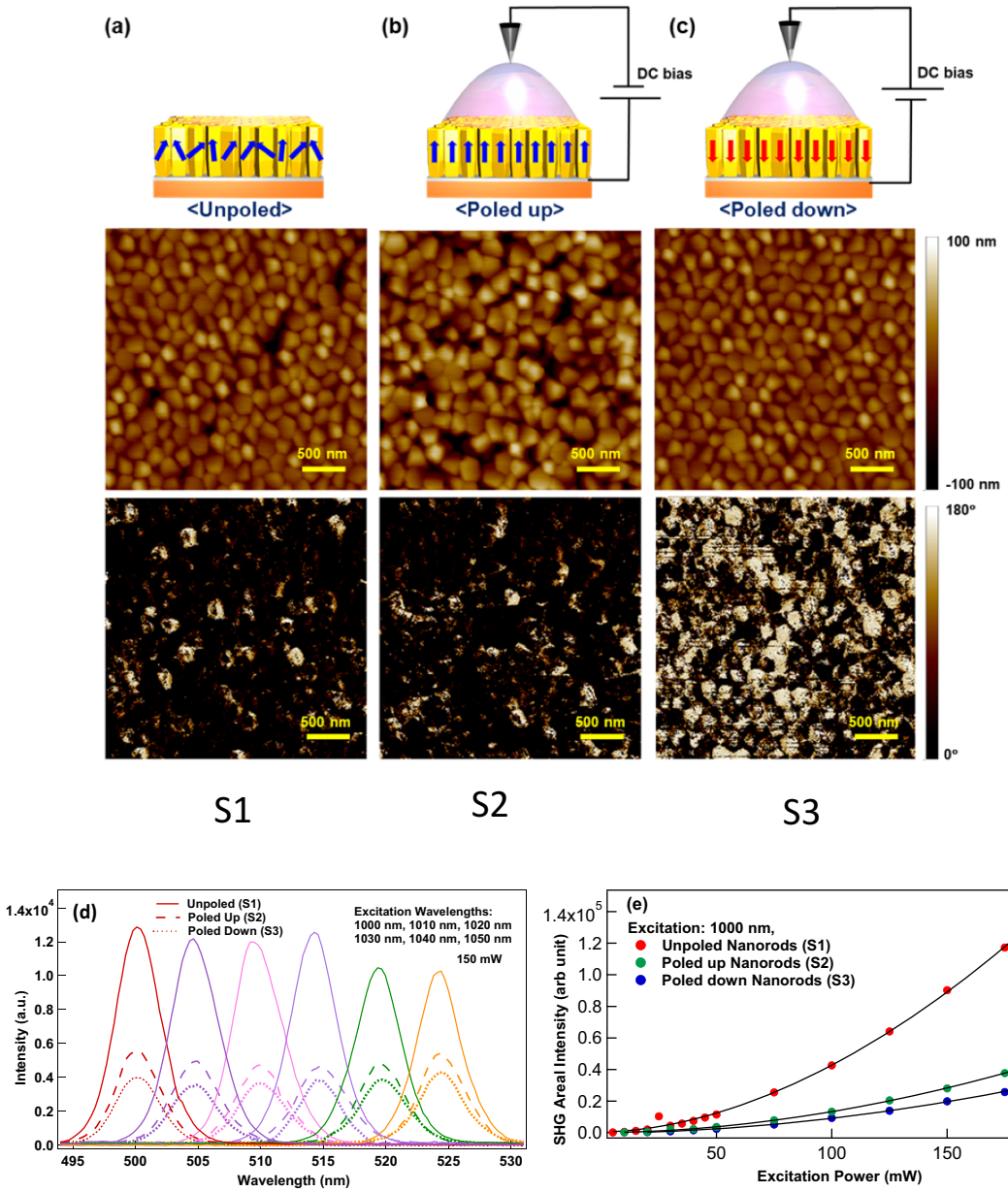

Figure 2. Piezoresponse force microscopy (PFM) images of PZT nanorod arrays with (a) unpoled, (b) poled up, (c) and poled down states. The images present both the topology (top panels) and phase signals indicating the polarization directions (lower panels) of the nanorods. The samples are different pieces from the same wafer. (d) The amplitude of SHG response for the unpoled (S1), poled up (S2), and poled down (S3) PZT nanorod arrays. (e) Power dependence of the samples show the SHG intensity is proportional to the square of the intensity of the incident light.

The SHG measurements at room temperature were probed, on both unpoled and poled nanorods from the same wafer. The piezoresponse force microscopy (PFM) response confirming the surface poling and is presented in figures 2(a)–(c). The initial polarization state of as-grown nanorods is the upward direction (out of plane). Without poling, the initial polarization of the nanorod arrays tend to most likely follow the growth direction (figure 2(a)); but the poling process is still required to align the polarization direction of the nanorods along the z-direction (figures 2(b) and (c)).

Our laser source was a Coherent Chameleon Ti:sapphire laser with a repetition rate of 80 MHz, and a pulse duration of 100 fs. We carried out measurements for wavelengths ranging from 690 nm to 1050 nm. The laser pulses were horizontally polarized (P-polarized). Figure 2(d) presents SHG on the three nanorod arrays, where the unpoled sample exhibited higher amplitudes under the same experimental conditions compared to the poled structures. Furthermore, the SHG intensity is expected to be proportional to the square of the intensity of the incident light (I_w^2). As shown in figure 2(e) we observe this quadratic dependence in all three samples.

In order to probe the differences between the poled and unpoled samples, in figure 3(a) we compare the SHG of sample S2 (poled up) under the exact experimental conditions before and after the sample was

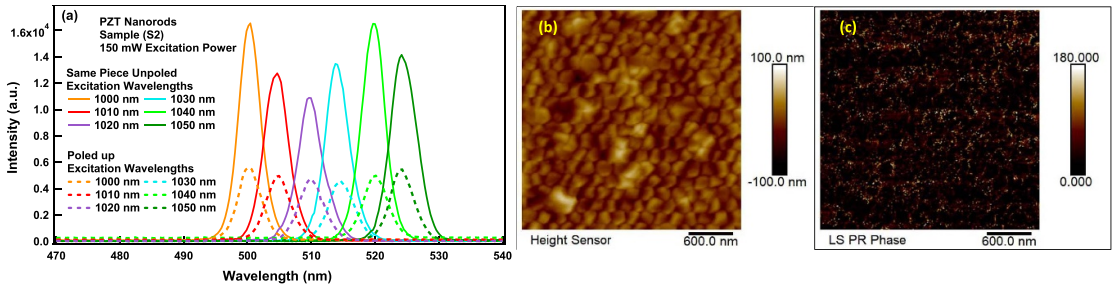

Figure 3. (a) The amplitude of the SHG for sample (S2) for when it was poled and then after it was heated to 400 °C. The measurements are under the exact same conditions. The SHG amplitude of the unpoled state of sample S2 is comparable to S1 (unpoled), in figure 2(d). (b) Topology from PFM measurements and (c) the phase of Sample S2, after it was heated to 400 °C for about 10 min, confirming the sample is unpoled after being heated.

heated to ∼400 °C to be unpoled. In Sample S2, the amplitude of the SHG, after heating is comparable to the SHG amplitude of sample S1 (unpoled), in figure 2(d). In figure 3(b), We also present the PFM images of the sample S2 after it was heated, demonstrating the sample is unpoled when the SHG was measured.

To provide some insights to the observed differences in the SHG amplitudes, we note that the phase-matching (PM) condition can play a role. For an isotropic crystal [38], SHG emitted from regions located within distances, comparable to the emission wavelength, can destructively interfere with each other. In disordered polycrystalline materials, a random quasi-phase-matching condition as an alternative method to enhance SHG conversion efficiency was demonstrated [39]. In their study, they reported that SHG resulted from different domains in a polycrystalline disordered structure, with nonidentical domain parameters (orientation, shape, and size), would acquire random phases [38, 39]. In a far field measurement such as our setup, when multiple randomly oriented single crystal domains exist and can be probed, one would expect that the interference would not be a major issue and thus the resultant SHG intensity is the sum of each SHG amplitudes from different domains [38, 40]. In Tetragonal $CH_3NH_3PbI_3$ the presence of multiple ferroelectric domains resulted in destructive interference between SHG scattered from domains with inverted polarity [41].

Furthermore, the coherence length, described as the distance in which the SHG intensity drops to zero due to destructive interference, depends on the excitation wavelength and the difference between the index of refraction associate with the SHG and the excitation wavelengths, in a given material [35, 40]. Therefore, in our samples, we would expect the amplitude of SHG to display some dependence on wavelengths and the overall orientation of the ferroic domains.

4. Polarization dependence

We also explored the polarization-dependence of SHG where the incident laser polarization was varied via a half-wave liquid crystal variable retarder/wave plate (Thorlabs; LCC1221-B), with an analyzer positioned before the spectrometer set at vertical (S) polarization. To test the sensitivity of the analyzer, we first used a 488 nm laser where the power plot as a function of polarization is presented in figure 4(a), showing a symmetric pattern.

Furthermore, figure 4(b) presents the polar plot with 980 nm, 200 mW incident power, for S1 (unpoled sample). Here we have constructed the polar plots using the area of the observed SHG peak as a function of incident light polarization. Compared to single-crystal systems, polycrystalline systems increase the complexity of determining the symmetry point groups of the material structure because, in a multi-domain system, the observed SHG intensity could be related to the net polarization of the domain pattern or the collective intensity of each contributing domain state [42].

Looking closer at the polarization dependence, as shown in figure 4(b), we observed a moderate dependence of the SHG intensity with respect to the incident polarization that displays four lobes. We note that in a previous work [43], PZT solid solutions with the composition close to $x = 0.47$ exhibited a morphotropic phase boundary with rhombohedral and tetragonal symmetries. Thus, the observed polar plot could result from the combination of the two phases in the PZT. Similar SHG observations have been reported in $BiFeO_3$ (BFO) films, where the authors have attributed the observed double lobed configuration to the combination of the monoclinic point group symmetry in BFO of each phase [42, 44]. Moreover, Wang *et al* [45] reported the SHG observation of non-zero minimum for thicker BFO films due to the overlapping of SHG signal generated from rhombohedral and tetragonal phases domains [45]. We should also note that

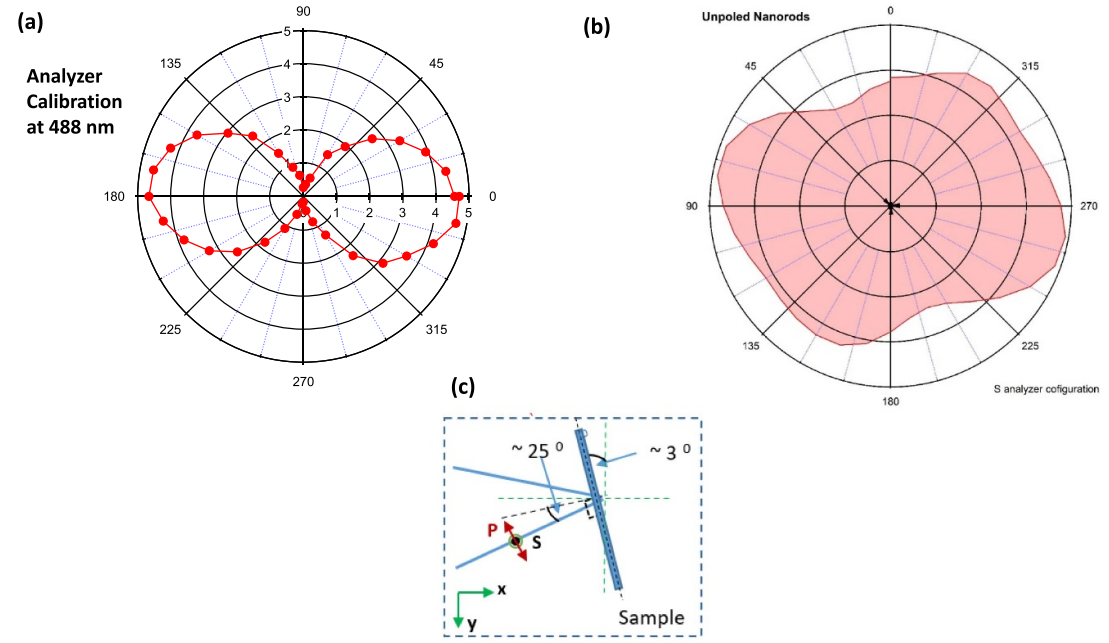

Figure 4. (a) Testing the analyzer sensitivity to polarization with a laser at 488 nm. The choice of this laser line was to be close to the SHG wavelengths. (b) The incident polarization dependence of SHG in the unpoled nanorod at 980 nm using an analyzer, with an analyzer set at S polarization on the emission path, similar to the measurements in panel (a). (c) The sample's orientation and the direction of the incident light where *xy* is referring to the table plane.

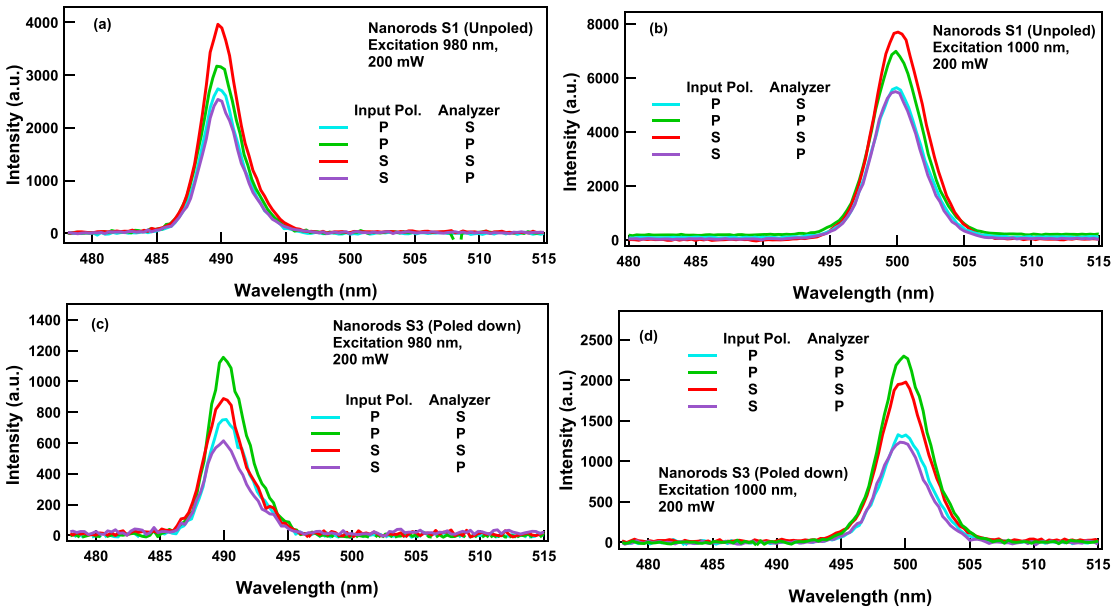

Figure 5. (a)–(d) The examples of the polarization dependence at 980 nm and 1000 nm for samples S1 and S3 with two different incident-analyzer arrangements (S or (P). In sample S1 (a) and (b) the S-S configuration resulted in the highest measured intensity and for sample S3 (c) and (d) P-P displayed the highest intensity.

the laser beam of ∼1 mm diameter covers a large number of individual nanorods; thus, the observed SHG could be an averaged intensity over multiple nanorods resulting in a less clearly resolved double lobed shape.

To show a few more examples of the polarization dependence in these nanorod arrays, figures 5(a)–(d) display SHG intensities, for two different excitation (S and P) and analyzer (S and P) configurations. These measurements were taken at 980 nm and 1000 nm under the exact same conditions. For all four configurations, the largest amplitude was measured when the excitation and analyzer polarizations were the same states. For the unpoled PZT sample (S1), S excitation polarization with S analyzer (S-S) configuration has the highest amplitude. In case of the poled down sample (S3) in figures 5(c)–(d), the P-P

configuration displayed the highest SHG emission. We should note that here the observed differences are due to the net polarization direction of the PZT nanorod arrays.

The second harmonic anisotropy pattern changes with the corresponding domain variant of the ferroelectric domain structure [46, 47]. The sample S1 (unpoled) has a net polarization direction to be partially upward whereas the net polarization direction sample S3 (poled down) is downward with respect to the sample structure, resulting in different in-plane and out-of-plane contributions to the final SHG amplitude. This results in different SHG anisotropy patterns with different intensities. Thus, the observed change in the SHG amplitude with the different incident polarizations and the analyzer configurations for the two samples (S1 and S3) could be due to the different in-plane out-of-plane contributions of each sample. Similarly in a recent study, Zhang *et al* [47] reported a significant difference in the shape and the intensity of the SHG polar pattern with different in-plane and out of plane domain components. In their study, the authors have illustrated the relationship between azimuth polarization dependent SHG signals and domain variants, for BFO, BTO, and PZT films. Moreover, they demonstrated that in-plane domain components were distinguished by analyzing the azimuth-polarization-dependent SHG patterns whereas out of plane domain components were analyzed by comparing the variation in the SHG patterns taken at the initial position (0°), and after rotating the sample 180° around sample plane. As shown in figure 4(c), we should note that for all the measurements presented here, the incident angle was kept ∼25° and the sample holder was tilted by about 3°.

5. Carrier relaxation dynamics in PZT nanorods

Ultrafast time-resolved spectroscopy can also be a useful tool for studying the energy relaxation processes and carrier dynamics in a wide variety of nanostructures. The extracted information can be used toward developing novel devices such as fast optical switches. Two types of ultrafast spectroscopy are commonly employed: time resolved differential transmission spectroscopy (TRDT) and TRDR. In carrier dynamics studies, TRDT measurements usually provide information on the exact energy state within a given band a carrier occupies and how it scatters into/out of that state. Photoexcited carriers within a given state block the absorption of further carriers through the Pauli exclusion principle (phase space filling). The TRDT signal is sensitive to all the photoexcited carriers throughout the entire thickness of the sample. TRDT measurements can provide detailed information on scattering rates from specific electronic states, but have the drawback that they are limited to thin samples (compared to the absorption depth) since the light must get through the sample.

In contrast to TRDT, transient reflectivity measurements depend upon the changes to the index of refraction that result from the photoexcited carriers. As a result, the TRDR measurements are not sensitive to the exact state within a band the photoexcited carrier occupies, but rather are sensitive to the effective mass of the bands, in which the carriers reside. Therefore, the scattering of a carrier *within* a band does not produce a change in the TRDR spectrum. Furthermore, the TRDR signal depends on the gradient of the change in the index of refraction due to the photoexcited carriers. This gradient is typically larger at the surface of the sample, and as a result, TRDR measurements studying carrier dynamics are mainly sensitive to the carriers near the surface [48, 49].

We employed TRDR and figure 6(a) displays degenerate pump/probe measurements at different NIR wavelengths, where we expected to observe multiphoton absorptions. The pump pulses had a spot size of 150–200 μm exciting multiple rods. For the carrier contribution, the TRDR signal, as noted above, is sensitive to the *photoexcited carriers at the surface* (or in layered structures, possibly at the interfaces). We should note that we required the maximum possible pump powers for the different NIR excitations to observe the multiphoton process, but these pump powers could not have been identical for each wavelength.

In TRDR, the differential reflection is related to the gradient of the change in the index of refraction that results from the pump pulse. This gradient is the largest when there is a discontinuity in the change of the index, such as at the surface or at the interface. The change in index comes about because, the carriers generated by the pump pulse, will change the real and imaginary parts of the dielectric function and hence, the index of refraction. As a result, TRDR measurements are sensitive to the density of photoexcited carriers near the surface of the sample. Photoexcited carriers can change the index of refraction in several ways. Some of the ways are described in detail by Zollner *et al* [48] which we just summarize here. They include: (a) Drude Model/induced free carrier absorption: Photoexcited carriers can screen internal electric fields and hence change the Drude part of the dielectric function (this is a photoinduced enhancement of the free carrier absorption). (b) Many body effects which include both the renormalization of the band gap by the photoexcited carriers as well as the change to the Coulomb enhancement of the optical matrix element arising from the screening of the photoexcited electron–hole Coulomb interaction by the other photoexcited carriers. (c) Phase space filling of the interband contribution to the dielectric function, which has a strong

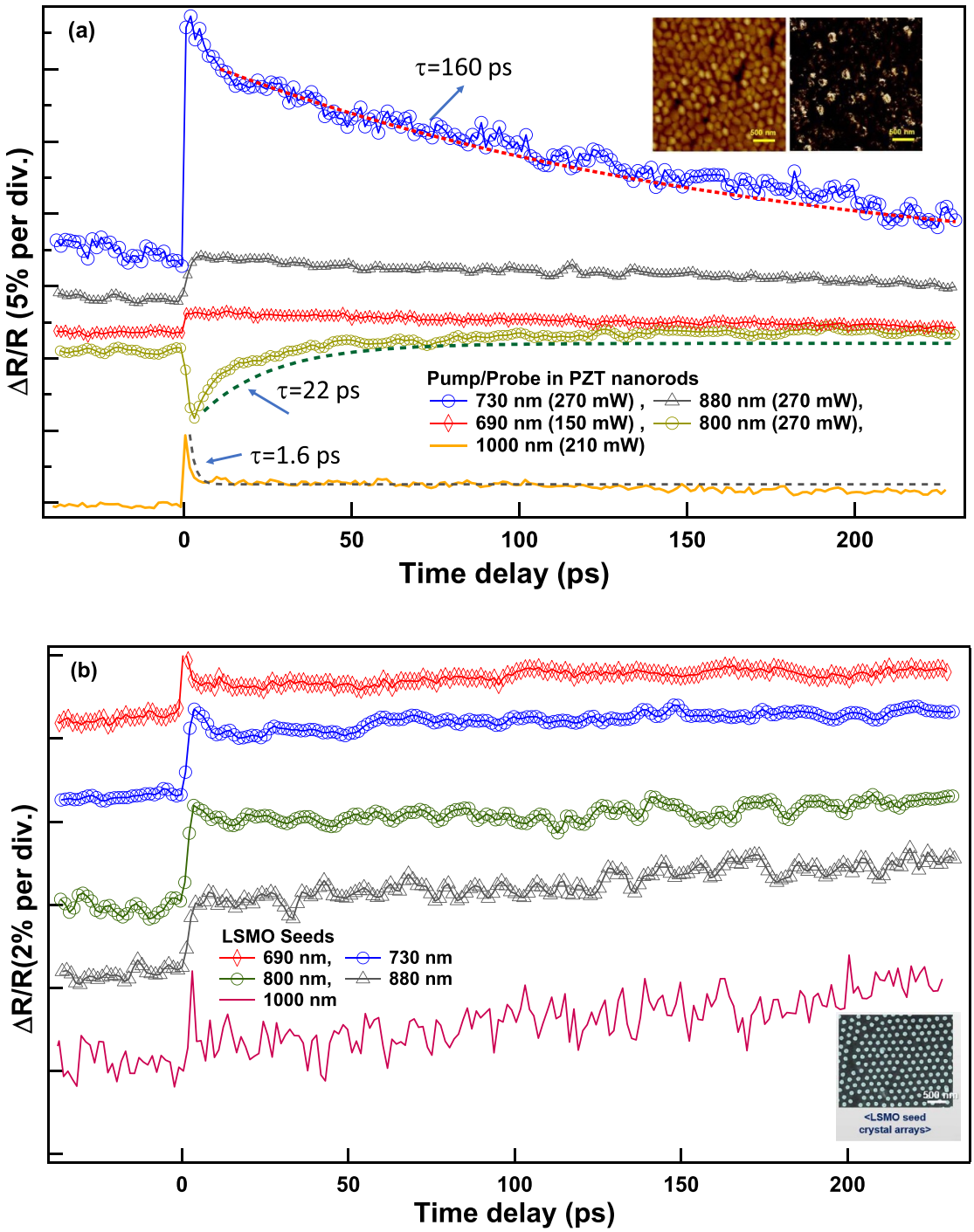

Figure 6. (a) Room temperature TRDR of PZT nanorods of the unpoled sample (S1). We observed carrier dynamics where both the pump/probe wavelengths were tuned in NIR. We should note, except at 800 nm, we observed an increase in the transient reflectivity, with the largest increase of ($\Delta R/R$) at 730 nm. The inset shows the topology and the phase of the nanorods. (b) Similar measurements on the LSMO seed show a much smaller response to the NIR optical excitations with no sensitivity to the variations in the excitation wavelengths. The inset displays the SEM image of the LSMO seeds to compare with the PZT nanorods' topology.

effect on the absorption and thus must also effect the index. While the first effect is considered to be the dominant effect, the relative importance will depend on the exact details of the electronic band structure of the material as well as the excitation wavelength of the pump laser pulse and the wavelength of the probe pulse.

Typical ways that the surface carrier dynamics can be altered include: (a) scattering of carriers at the surface to *different bands* (with different effective masses), (b) recombination of photoexcited carriers (across the gap), (c) diffusion of photoexcited of carriers away from the surface (including possible drift effects if there are internal fields) [48, 49] and (d) trapping/recombination of carriers at surface/interfaces. The thickness of layered structures can also influence the relaxation dynamics. More specifically, for thin layers,

photoexcited electrons can reach a surface or interface and recombine with the surface states in a few picoseconds without any radiative or thermal recombination. Carrier dynamics in InN nanorod arrays demonstrated wavelength dependence, and similar to our observations the sign change of $\Delta R/R$ was attributed to nonlinear effects such as band gap renormalization and the bleaching of the absorption near the absorption edge [50].

Since the band gap of PZT (∼3.4 eV) is greater than the excitation energy of the laser pump pulse, the absorption depth is fairly large ≈0.5–1.0 μm or more, one initially might not expect diffusion to play a role. However, the dominant method of photoexcitation is not through *single* photon absorption, but is instead through *two* photon (or multi-photon) absorption. It is well known, that carriers generated by two (or multiple) photon absorption can be highly spatially confined or localized. Depending on the focus, this is typically near the surface, and this fact allows one to investigate carrier dynamics and transport in these systems. As carriers generated near the surface they can diffuse into the sample.

Our observation of TRDR in the nanorods with the photoexcited carriers generated along the rods, could be more complex than what one would expect in films, specially when multiphoton processes are involved. Furthermore, the additional surface area of the nanorods could lead to a larger number of surface traps/defects which in turn could affect the carrier relaxation dynamics. As shown in the figure 6(a), in the case of the pump/probe at 800 nm, the dynamics start with a negative rise in the $\Delta R/R$ where the decrease at timing zero can be attributed to the Pauli blocking when conduction states fill up, causing the refractive index to decrease, resulting in a negative $\Delta R/R$. The dynamics at this pump/probe scheme can be fitted with one single exponential decay with the time constant of 22 ps.

For the pump/probe excitations at 690 nm and 880 nm, we observed positive changes in $\Delta R/R$ followed by decays characterized by slow time constants. The slow relaxation phenomena are typically attributed to carrier diffusion where there will be a large positive offset at long time delays. In this case, all the absorbed energy could heat up the lattice indicating a slow thermal diffusion in these two pump/probe cases. Furthermore, for excitation at 730 nm and 1000 nm with positive changes in $\Delta R/R$, we can describe the relaxation with a single exponential fit resulting in decay component of 160 ps and 1.6 ps, respectively.

The sensitivity of the carrier dynamics to the excitation wavelength was reported in GaAs [51]. In their work, they observed an increase in the initial differential reflectivity for the incident pump wavelengths of 820, 875, and 880 nm and a decrease for 885 nm. Their observations of the sign changes in $\Delta R/R$ were consistent with the theoretical investigations of refractive index nonlinearities near the bandgap of GaAs. They associate the near band edge transient nonlinear optical response, to band-gap renormalization where the excitation energies were near bandgap. In our study, the incident wavelengths 690–1000 nm (1.80–1.24 eV), are below the bandgap for PZT nanorods of 3.4 eV [52]. But for two or three photon absorption, can either be above the band gap, or close to the band gap.

Thus, we observe several multiphoton processes in these measurements. At 690 nm (1.80 eV) it requires at least two photons to excite a charge carrier into the conduction band via an intermediate state. Similarly, at 1000 nm (1.24 eV) it requires at least three photons to excite carriers into the conduction band via an intermediate state. Although we did not expect the pump/probe excitations could reach to the substrate, we tested the bare LSMO patterned on top of Pt coated Si(100) substrate. As shown in figure 6(b) the observed dynamics for the substrate are different under the exact experimental conditions as the ones for the nanorods, and we observed only a small response, with no sensitivity to the excitation wavelengths. This fact confirms that the multiphoton excitations are mainly probing highly localized states of the nanorods near the surface.

Furthermore, as shown in figure 7 in order to probe the interband relaxation time scale, we used pump pulses closer to the bandgap of the PZT nanorods and we employed a two-color pump-probe scheme [49]. The pump and probe wavelengths were 400 nm and 800 nm, respectively where we used an amplified Ti:sapphire system with a repetition rate of 1 KHz. Our laser spot size was ∼150 μm in diameter with a pump power of 1 mW, and a pump/probe ratio of 1000:1. In this scheme, we used a BBO non-linear crystal to upconvert the pump pulses from 800 to 400 nm. We observed a much smaller amplitude of $\Delta R/R$, with an initial sharp increase at the timing zero, followed by a slower increase. This fact suggests that the 400 nm pump pulse creates carriers in higher energy bands and the 800 nm pulses probe lower energy bands, which see an increase in carrier density, as the carriers in higher energy bands relax. This is similar to what is seen in Ge where one sees scattering and relaxation from the light hole bands to the heavy hole bands (figure 1(b) in Zollner *et al* [48]).

We note that the photoexcited carrier lifetime is much longer than the cases presented in figure 6(a), created via two or three photon processes. In this two color scheme the initial slow relaxation, is attributed to the carrier lattice heating (10–100 picoseconds) followed by an interband relaxation process of large carrier population (lasting ∼1 ns), after the initial thermalization. In addition, in the two color scheme, at 1 ns; $\Delta R/R$ changes sign, where we expected the system should have reached to equilibrium.

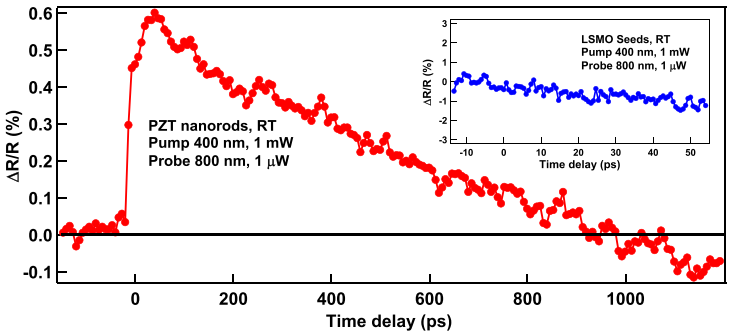

Figure 7. The TRDR of the nanorods in a two color scheme where the pump tuned at 400 nm, is close to the expected bandgap of PZT. The inset shows the two color pump/probe measurements on the LSMO seeds for the same experimental condition.

6. Conclusion

Our optical characterizations presented in this study, provide new directions to employ PZT nanorods, with enhanced piezoelectric and ferroelectric performance, for devices on the basis of SHG when low dimensionality and compatibility to Si are desirable. The choice of PZT, with a bandgap of ∼3.4 eV, has the additional advantage of avoiding the re-absorption of the SHG emissions in the observed range of (2.36–2.5 eV). Employing nonlinear optical processes at the nanoscale can play important roles in quantum optics, information technology, and in the development of new light sources.

Furthermore, we used TRDR spectroscopy to study the carrier dynamics of the nanorods. Probing, both close to the bandgap, as well as through multiphoton processes allowed us to identify several different relaxation mechanisms. The TRDR through multiphoton excitations displayed strong wavelength dependence, where the dynamics are typically occurring near the surface and the relaxation processes can be dominated by carrier diffusion. Moreover, we used near gap excitation at 400 nm to identify the interband relaxation time scale, and estimated to be about 1 ns. These results provide insights for different paths toward optical manipulation of these less explored PZT nanorods in time domain; suggesting that they have potentials for fast optoelectronic applications. The possibility of employing NIR excitation provide an opportunity, to go beyond traditional visible spectroscopy, in which multiphoton time resolved spectroscopy can shade light to new and important dynamical mechanisms.

Data availability statement

The data that support the findings of this study are available upon reasonable request from the authors.

Acknowledgment

This material is based upon work supported by the Air Force Office of Scientific Research under Award No. FA9550-17-1-0341 and DURIP funding (FA9550-16-1-0358). Kiara McMillan and Ada Morral acknowledge the support from Clare Boothe Luce Program at Virginia Tech.

ORCID iDs

Shashank Priya https://orcid.org/0000-0003-1367-3434
Christopher J Stanton https://orcid.org/0000-0002-0551-4989
Giti A Khodaparast https://orcid.org/0000-0002-1597-6538

References

[1] Keller U 2003 Recent developments in compact ultrafast lasers *Nature* **424** 831–8
[2] Li W *et al* 2014 Ultrafast all-optical graphene modulator *Nano Lett.* **14** 955–9
[3] Schönenberger S *et al* 2010 Ultrafast all-optical modulator with femtojoule absorbed switching energy in silicon-on-insulator *Opt. Express* **18** 22485–96
[4] Ray P C 2010 Size and shape dependent second order nonlinear optical properties of nanomaterials and their application in biological and chemical sensing *Chem. Rev.* **110** 5332–65
[5] Campagnola P J, Wei M D, Lewis A and Loew L M 1999 High-resolution nonlinear optical imaging of live cells by second harmonic generation *Biophys. J.* **77** 3341–9

[6] Shen Y R 1989 Surface properties probed by second-harmonic and sum-frequency generation *Nature* **337** 519–25
[7] Zhuang X, Miranda P B, Kim D and Shen Y R 1999 Mapping molecular orientation and conformation at interfaces by surface nonlinear optics *Phys. Rev.* B **59** 12632–40
[8] Bonacina L, Brevet P-Fçois, Finazzi M and Celebrano M 2020 Harmonic generation at the nanoscale *J. Appl. Phys.* **127** 230901
[9] Yamashitaa S 2019 Nonlinear optics in carbon nanotube, graphene and related 2D materials *APL Photonics* **4** 034301
[10] Wu L *et al* 2019 Kerr nonlinearity in 2D graphdiyne for passive photonic diodes *Adv. Mater.* **31** 1807981
[11] Jiang X *et al* 2018 Ultrathin metal–organic framework: an emerging broadband nonlinear optical material for ultrafast photonics *Adv. Opt. Mater.* **6** 1800561
[12] Lu L *et al* 2017 Broadband nonlinear optical response in few-layer antimonene and antimonene quantum dots: a promising optical kerr media with enhanced stability *Adv. Opt. Mater.* **5** 1700301
[13] Jiang X, Kuklin A V, Baev A, Ge Y, Ågren H, Zhang H and Prasad P N 2020 Two-dimensional MXenes: from morphological to optical, electric and magnetic properties and applications *Phys. Rep.* **848** 1–58
[14] Mennel L, Paur M and Mueller T 2019 Second harmonic generation in strained transition metal dichalcogenide monolayers: MoS_2, $MoSe_2$, WS_2 and WSe_2 *APL Photonics* **4** 034404
[15] Koka A and Sodano H A 2013 High-sensitivity accelerometer composed of ultra-long vertically aligned barium titanate nanowire arrays *Nat. Commun.* **4** 2682
[16] Wang X 2012 Piezoelectric nanogenerators–harvesting ambient mechanical energy at the nanometer scale *Nano Energy* **1** 13–24
[17] Kushnir U and Rabinovitch O 2009 Advanced piezoelectric–ferroelectric stack actuator *Sens. Actuators* A **150** 102–9
[18] Flynn A M, Tavrow L S, Bart S F, Brooks R A, Ehrlich D J, Udayakumar K R and Cross L E 1990 Piezoelectric micromotors for microrobots *IEEE Symp. Ultrason.* **3** 1163–72
[19] Fujii T, Watanabe S, Suzuki M and Fujiu T 1995 Application of lead zirconate titanate thin film displacement sensors for the atomic force microscope *J. Vac. Sci. Technol.* B **13** 1119–22
[20] Luginbuhl P, Racine G-A, Lerch P, Romanowicz B, Brooks K G, de Rooij N F, Renaud P and Setter N 1996 Piezoelectric cantilever beams actuated by PZT sol-gel thin film *Sens. Actuators* A **54** 530–5
[21] Riza N A, Polla D L, Robbins W P and Glumac D E 1993 High resolution 50 nm linear displacement macroscale meander-line PZT actuator *Electron. Lett.* **29** 1606–8
[22] Bernstein J J, Finberg S L, Houston K, Niles L C, Chen H D, Cross L E, Li K K and Udayakumar K 1997 Micromachined high frequency ferroelectric sonar transducers *IEEE Trans. Ultrason. Ferroelectr. Freq. Control* **44** 960–9
[23] Chen Xi, Xu S, Yao N and Shi Y 2010 1.6 V nanogenerator for mechanical energy harvesting using PZT nanofibers *Nano Lett.* **10** 2133–7
[24] Kang P G, Lee T K, Ahn C W, Kim I W, Lee H H, Choi S B, Sung K D and Jung J H 2015 Vertically aligned epitaxial $KNbO_3$ nanorod array for piezoelectric energy harvester and second harmonic generator *Nano Energy* **17** 261–8
[25] Koka A and Sodano H A 2014 A low-frequency energy harvester from ultralong, vertically aligned $BaTiO_3$ nanowire arrays *Adv. Energy Mater.* **4** 1301660
[26] Gu L *et al* 2013 Flexible fiber nanogenerator with 209 V output voltage directly powers a light-emitting diode *Nano Lett.* **13** 91–4
[27] Wu W, Bai S, Yuan M, Qin Y, Wang Z L and Jing T 2012 Lead zirconate titanate nanowire textile nanogenerator for wearable energy-harvesting and self-powered devices *ACS Nano* **6** 6231–5
[28] Xu S, Hansen B J and Wang Z L 2010 Piezoelectric-nanowire-enabled power source for driving wireless microelectronics *Nat. Commun.* **1** 93
[29] Wang X 2012 Piezoelectric nanogenerators–harvesting ambient mechanical energy at the nanometer scale *Nano Energy* **1** 13–24
[30] Janshoff A, Galla H-J and Steinem C 2000 Piezoelectric mass-sensing devices as biosensors–an alternative to optical biosensors? *Angew. Chem., Int. Ed. Engl.* **39** 4004–32
[31] Kang M G, Lee S-Y, Maurya D, Winkler C, Song H-C, Moore R B, Sanghadasa M and Priya S 2017 Wafer-scale single-crystalline ferroelectric perovskite nanorod arrays *Adv. Funct. Mater.* **27** 1701542
[32] Son J Y, Lee J-H, Song S, Shin Y-H and Jang H M 2013 Four-states multiferroic memory embodied using Mn-doped $BaTiO_3$ nanorods *ACS Nano* **7** 5522–9
[33] Tang Y-Y, Zhang W-Y, Li P-F, Ye H-Y, You Y-M and Xiong R-G 2016 Ultrafast polarization switching in a biaxial molecular ferroelectric thin film: $[Hdabco]ClO_4$ *J. Am. Chem. Soc.* **138** 15784–9
[34] Kang M G K, Kang H B K, Clavel M, Maurya D, Gollapudi S, Hudait M, Sanghadasa M and Priya S 2018 Magnetic field sensing by exploiting giant nonstrain-mediated magnetodielectric response in epitaxial composites *Nano Lett.* **18** 2835–43
[35] Denev S A, Lummen T T A, Barnes E, Kumar A and Gopalan V 2011 Probing ferroelectrics using optical second harmonic generation *J. Am. Ceram. Soc.* **94** 2699–727
[36] Larciprete M C and Centini M 2015 Second harmonic generation from ZnO films and nanostructures *Appl. Phys. Rev.* **2** 031302
[37] Dang Y, Zhong C, Zhang G, Ju D, Wang L, Xia S, Xia H and Tao X 2016 Investigations into properties of acentric hybrid perovskite single crystals $NH(CH_3)_3SnX_3$ (X = Cl, Br) *Chem. Mater.* **28** 6968
[38] Skipetrov S E 2004 Disorder is the new order *Nature* **432** 285
[39] Baudrier-Raybaut M, Haïdar R, Lemasson P, Kupecek P and Rosencher E 2004 Random quasi-phase-matching in bulk polycrystalline isotropic nonlinear material *Nature* **432** 374
[40] Miller R C 1964 Optical harmonic generation in single crystal $BaTiO_3$ *Phys. Rev.* **134** A1313
[41] Rakitaa Y *et al* 2017 Tetragonal $CH_3NH_3PbI_3$ is ferroelectric *Proc. Natl Acad. Sci.* **114** E5504
[42] Trassin M, De Luca G, Manz S and Fiebig M 2015 Probing ferroelectric domain engineering in $BiFeO_3$ thin films by second harmonic generation *Adv. Mater.* **27** 4871–6
[43] Noheda B, Gonzalo J A, Cross L E, Guo R, Cox D E, Park S-E and Shiran G 2000 Tetragonal-to-monoclinic phase transition in a ferroelectric perovskite: the structure of $PbZr_{0.52}Ti_{0.48}O_3$ *Phys. Rev.* B **61** 8687
[44] Kumar A, Denev S, Zeches R J, Vlahos E, Podraza N J, Melville A, Schlom D G, Ramesh R and Gopalan V 2010 Probing mixed tetragonal/rhombohedral-like monoclinic phases in strained bismuth ferrite films by optical second harmonic generation *Appl. Phys. Lett.* **97** 112903
[45] Wang J-S, Jin K-J, Guo H-Z, Gu J-X, Wan Q, He X, Li X-L, Xu X-L and Yang G-Z 2016 Evolution of structural distortion in $BiFeO_3$ thin films probed by second-harmonic generation *Sci. Rep.* **6** 38268
[46] Wang J-S, Jin K-J, Gu J-X, Wan Q, Yao H-B and Yang G-Z 2017 Direct evidence of correlation between the second harmonic generation anisotropy patterns and the polarization orientation of perovskite ferroelectric *Sci. Rep.* **7** 9502
[47] Zhang Y *et al* 2018 Characterization of domain distributions by second harmonic generation in ferroelectrics *npj Comput. Mater.* **4** 39

[48] Zollner S, Myers K D, Dolan J M, Bailey D W and Stanton C J 1998 Theory of femtosecond ellipsometry in Ge at 1.5 eV *Thin Solid Films* **568** 313–14
[49] Mudiyanselage R R H H *et al* 2019 Coherent acoustic phonons and ultrafast carrier dynamics in hetero-epitaxial $BaTiO_3$–$BiFeO_3$ films and nanorods *J. Mater. Chem.* C **7** 14212–22
[50] Ahn H, Yu C, Yu P, Tang J, Hong Y and Gwo S 2012 Carrier dynamics in InN nanorod arrays *Opt. Express* **20** 769
[51] Janz S, Akano U G and Mitchell I V 1996 Nonlinear optical response of As^+-ion implanted GaAs studied using time resolved reflectivity *Appl. Phys. Lett.* **68** 3287–9
[52] Pandey S K, James A R, Raman R, Chatterjee S N, Goyal A, Prakash C and Goel T C 2005 Structural, ferroelectric and optical properties of PZT thin films *Physica* b **369** 135–42